PAPER • OPEN ACCESS
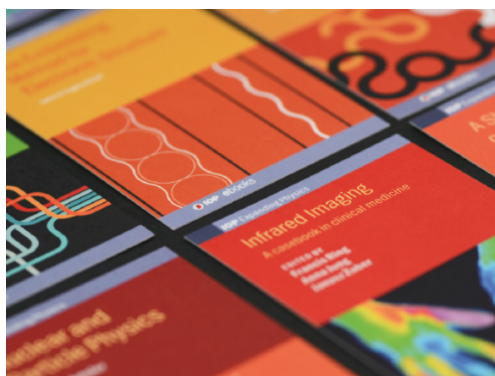
The role of geometry in the generation of a shock wave by a femtosecond laser pulse

View the article online for updates and enhancements.

The role of geometry in the generation of a shock wave by a femtosecond laser pulse

V V Shepelev[1], N A Inogamov[2,3] and S V Fortova[1]

[1] Institute for Computer-Aided Design of the Russian Academy of Sciences, Vtoraya Brestskaya 19/18, Moscow 123056, Russia

[2] Landau Institute for Theoretical Physics of the Russian Academy of Sciences, Akademika Semenova 1a, Chernogolovka, Moscow Region 142432, Russia

[3] Dukhov Research Institute of Automatics (VNIIA), Sushchevskaya 22, Moscow 127055, Russia

E-mail: `vadim.aries@gmail.com`

Abstract. Laser exposure at a sufficient intensity creates a shock wave (SW), propagating in the irradiated target. The process is used in many technological applications. As a result of femtosecond exposure, a warmed up layer with a thickness of $d_\mathrm{T} \sim 0.1$ μm occurs. The radius of the heating spot R_L varies from values of the order of a micron (focusing on the diffraction limit) up to tens or hundreds of microns depending on the experiment. As you can see, $R_\mathrm{L} \gg d_\mathrm{T}$, therefore one-dimensional motion with a plane surface is generated. The quasi-plane SW stage ends when the SW moves away from the target surface to a depth of about R_L. Then the stage of quasi-hemispherical propagation begins. The paper analyzes the transition from plane to hemispherical SW. The motion of the "wings" of a hemispherical wave on the target surface bordering on a gas or vacuum is investigated. Theoretical estimates and numerical simulation results are presented. Analysis of the movement of the "wings" on the surface is important for experimental diagnostics of phenomena inside the target.

1. Introduction
Lasers are used as a tool in many industrial applications, such as follows:

- Strengthening of materials by passing a shock wave (SW) [1–6] known as laser shock peening (LSP), increased resistance to corrosion and wear due to fatigue.
- The formation of colloids of nanoparticles by means of laser ablation in liquid (LAL) [7–22]. We emphasize that LSP and LAL are two sides of the same coin. In case of LSP, they are interested in SW and what is happening inside the target, and in case of LAL, they analyze the substance ejected from the target. In both cases, the effect on the target through a transparent liquid is usually considered.
- Additive technologies [23, 24].
- Structuring of the surface [18, 25–32]. There are modes of influence, after which there are chaotic structures on the surface [25, 26, 28], and modes, in which periodic structures are formed [30]—laser induced periodic surface structures (LIPSS).

Two other important fields of application of laser-generated SWs are primarily related to the fundamental study of the equations of state (EOS) of substances in wide areas of their phase

diagram [33–35]; these areas also include extreme states of matter. Secondly, strength properties of condensed media is studied using lasers and SW [34, 36–39]. Previously for LSP, LAL, and thermodynamic equations of state investigation [33, 35] nanosecond pulses were used. For sintering or melting powders [23, 24] or cutting metals [40, 41] continuous lasers [42] are used.

Situation in industry and research has changed dramatically with the advent of ultra short pulse lasers; Gerard Moore and Donna Strickland were awarded Nobel prize in 2018 for creating such light sources. The fact is that the physics of the interaction of laser radiation with matter has changed fundamentally when pulse is shortened by 3–5 orders of magnitude from nanoseconds to tens of femtoseconds and units of picoseconds. There are three qualitative factors that sharply distinguish ablation using ultrashort pulse lasers from that in nanosecond case.

First, separation of the electron temperature from the phonon temperature becomes essential. The fact is that the laser transmits energy to electrons, and the transfer of absorbed energy to lattice is relatively slow. The weak thermal coupling of electrons and ions is due to the huge difference in mass. These circumstances were taken into account in the pioneering work of 1974 Anisimov with co-authors [43]. Work [43], which laid the Foundation of the two-temperature model, is for many years ahead of the work of Moore and Strickland on femtosecond lasers.

The second and third circumstances are related to, that the laser energy release begins and ends inside the condensed phase. That is, the heating layer with a thickness of d_T does not have time to expand (unload) hydrodynamically before the end of the heating process. As a result, pressure in the d_T-layer increases dramatically [44].

According to d'Alembert solution of linear acoustics, from the d_T-layer of high pressure two acoustic waves begin their propagation, which "take out" high pressure from the d_T-layer. One of these waves runs into the target, and the other—to the surface of the target [44]. This situation is qualitatively different in hydrodynamic terms from the situation in case of nanosecond pulses, see [5, 45]. In case of d'Alembert solution, acoustic disturbances run through the condensed phase. Whereas with a nanosecond impact, there is a "piston", which separates hot gas (plasma) phase and condensed phase. Vapor pressure of the vaporized substance or pressure of the plasma corona forces the piston to press on the condensed phase. Characteristics emitted by the piston go far into thickness of the target, forming extended compression wave. Whereas for femtosecond exposure, wave thickness is small: this thickness is of the order of d_T.

The second of the three circumstances that distinguish femtosecond (fs) and nanosecond (ns) effects is associated with a simple Riemann wave running to the boundary of the target with vacuum. This wave, reflecting from the vacuum boundary, changes the property—namely, from compression wave $p > 0$ turns into stretching wave $p < 0$. Stretching (at an amplitude higher than the ablation threshold) results in separation of the condensed phase layer from the target. That is, instead of evaporation, there is a separation of a macroscopic piece of condensed phase.

Let us explain that in ns ablation, the entrainment (ablation) of a substance occurs due to the transfer of the substance from a condensed state to gas (plasma) state. So, fs-ablation has a threshold and carries away a layer (shell) of condensed matter. Existence of a flying shell was discovered in works [46, 47]. Shell concept explains what observations of Newton's rings multiplying over time are related to [46, 47].

The third circumstance is connected with a simple Riemann wave running into the thickness of the target. This is compression wave. At initial stages, its thickness is about d_T. Due to non-linearity, after passing a certain distance of the run, the wave overturns—formation of triangular wave begins. The shorter the distance, the higher wave amplitude at the initial stage is. Then the triangular SW widens, and its amplitude decreases approximately according to law

$$p \propto u \propto 1/\sqrt{t} \propto 1/\sqrt{z} \tag{1}$$

(see [48, chapter 10]) as long as the SW is quasi-plane; the front of the quasi-plane SW is shown by curve 1 in figure 1. Such a dependence takes place due to non-linearity of inertial term $u\nabla u$
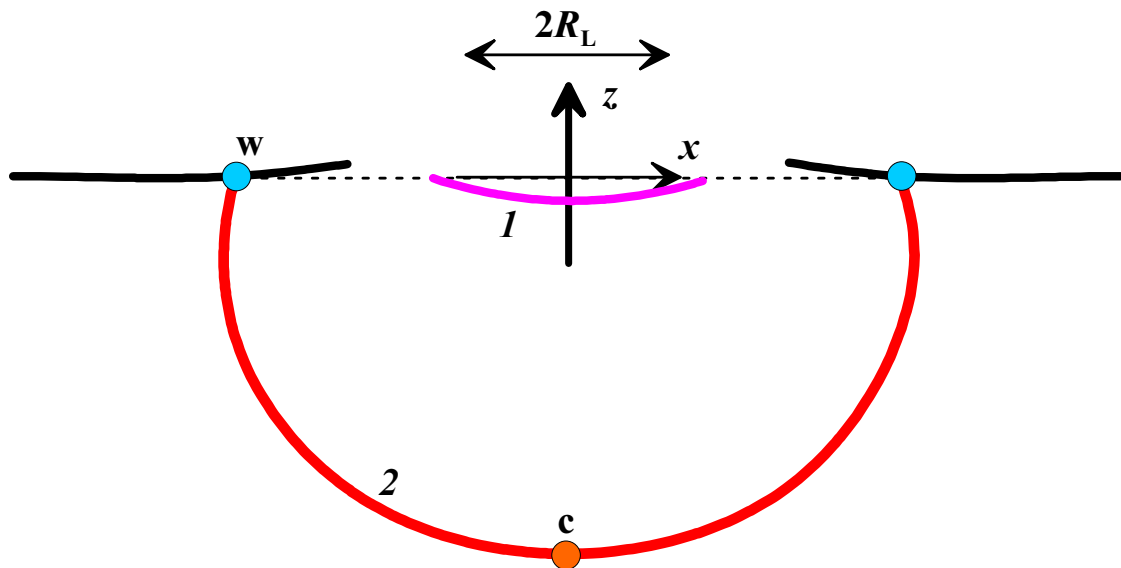
Figure 1. The scheme of action of an ultrashort laser pulse. The pulse creates a thin warmed up d_T-layer ($d_T \ll R_L$) at the surface. This layer is also a high-pressure layer at the initial stage. Decay of the high-pressure layer along the d'Alembert forms a quasi-plane characteristic *1*, propagating into the target volume. With a strong impact, a quasi-plane SW *1* runs ahead. At the propagation distances of this SW in depth of the order of the laser beam radius $z_c \approx R_L$ a quasi-plane SW (front of SW *1*) is transformed into a quasi-hemispherical SW (front SW *2*). In this case, the attenuation of SW increases sharply due to spatial divergence. Due to the presence of a free boundary (the boundary of the target with vacuum), wave amplitude decreases from the point "c" to the point "w". At the "w" point, the slash line is adjacent to the border.

and to dependence of sound speed on pressure. In (1), value $z \approx c_s t$ is the distance traveled by the SW during t. It is the study of evolution of this kind of shock waves (taking into account the geometry) that is a subject of this paper.

What is new in this paper is related to analysis of geometry effects. Irradiation of the target with a laser beam with a diameter of $2R_L$ is shown in figure 1.

In the course of evolution, a transition occurs from quasi-plane (curve 1 in figure 1) to quasi-hemispherical (curve 2 in figure 1) distribution mode.

Hemispherical front 2 in figure 1 is not an exact hemisphere; this would be asymptotic for $|z_c| \gg R_L$, if boundary with vacuum is replaced by absolutely rigid (non-deformable) plane. The shape of SW 2 is affected by presence of a close boundary with vacuum. One the consequences of this is presence of a circle "w", where oblique SW comes to surface, see figure 1. After the point "w", a Prandtl–Mayer flow type occurs, in which substance not only moves in the direction of SW, but also begins to expand in the direction of vacuum (rotation of the flow).

In addition to two acoustic waves (modes), an entropy mode is created when the laser pulse is applied with the formation of a hot d_T-layer. Acoustic waves propagate relative to the substance. Their speed is high, equal to speed of sound c_s. Entropy mode moves slowly with matter. The values of high entropy are "frozen" in the material of the d_T-layer. At acoustic time scale $t_s = d_T/c_s$ d'Alembert waves leave the hot d_T-layer, which remains as a high-entropy trace of laser action.

An interesting question concerns a complex dimensionless flow, in which the moving matter of the entropy trace is adjacent to relatively cold substance left by the diverging SW; see main text for this.
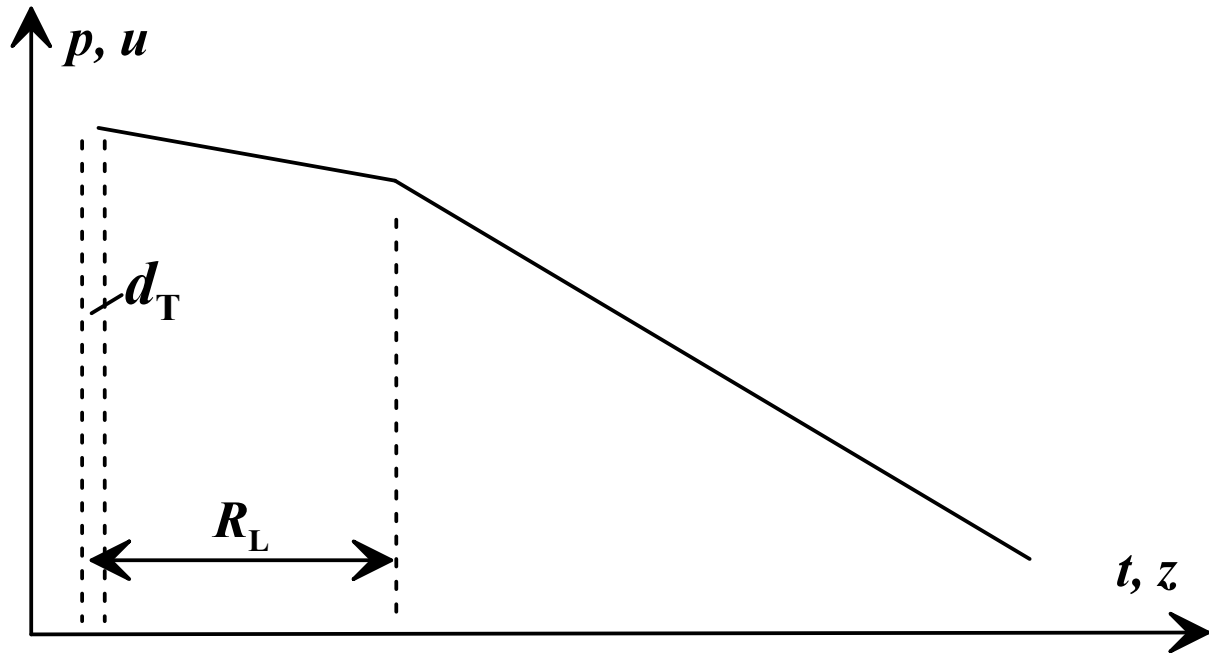
Figure 2. Changing the SW attenuation modes with a distance of z or a time of t. The values p, u are pressure and velocity values immediately behind the SW front at the central point "c" shown in figure 1. The mode change occurs at $z \approx R_L$ or at times $t_L \approx R_L/c_s$.

We will be interested in both case of cylindrical lens and case of spherical lens focusing light beam $2R_L$ on target surface, see figure 1. Cylindrical lens (its axis is perpendicular to the plane of figure 1) corresponds to plane 2D geometry. In this geometry, current lines of motion are situated in the plane of figure 1. At $|z_c| > R_L$, due to divergence, the SW amplitude decreases faster than according to law (1). For quasi-flat propagation of SW, pressure decreases according to law (1). This degree estimate is valid up to pressures of the order $B \sim 1$ Mbar, where B is volume compression module. At ultrahigh pressures $p \gg B$, the situation is similar to one that occurs in short impact problem [49]. SW attenuation increases when switching to a short shock: instead of 1/2 degree (non-linearity and dispersion), degrees are obtained in a range from 2/3 to 1, depending on the adiabatic index. The range boundaries are related to laws of conservation of momentum (value 1) and energy (value 2/3) [49].

In future, this study will allow for observations from above for the side SW "w" in figure 1 judge what is happening in target thickness at depths of the order of z_c; this is important for understanding LSP processes.

Structure of the article is as follows. First, we give estimates of SW attenuation at propagation distances in metal volume less than $z_c < R_L$ and greater than $z_c > R_L$ of the beam radius. Next, we give estimates of pressures in typical experiments. Then we describe the results of numerical simulation.

2. Changing attenuation mode at depth of the order of the laser beam radius

Change in the attenuation mode is caused by change in the propagation geometry of the SW. This is shown in figure 1. Corresponding change in the dependence of the amplitude decrease on time or on the path of propagation of the head wave is shown schematically in figure 2. As mentioned above, SW is formed as a result of overturning one of two d'Alembert waves after leaving warmed up d_T-layer.

Table 1. Classification of modes depending on geometry and role of cohesion.

Geometry	$p < B$	$p > B$
1D	β_1^{low}	β_1^{high}
2D, 3D	$\beta_{2.3}^{\text{low}}$	$\beta_{2.3}^{\text{high}}$

Let initial amplitude of the SW (i.e., in the area of $z \approx d_{\text{T}}$) be p_{T}. There are two propagation modes: flat one-dimensional (1D) and divergent two- or three-dimensional (2D, 3D). And there are two ranges of amplitudes: less and more than volume module $B \sim 1$ Mbar.

Divergent mode follows flat mode in time, see figures 1 and 2. The SW divergence occurs in two geometries associated with illumination by cylindrical (2D geometry x, z) and spherical (3D geometry x, y, z) lenses, see figure 1 and section 1. On a section of quasi-flat SW $d_{\text{T}} < z < R_{\text{L}}$, pressure decreases approximately according to law

$$p \propto p_{\text{T}}(d_{\text{T}}/z)^{\beta_1} \propto p_{\text{T}}(t_{\text{s}}/t)^{\gamma_1}, \tag{2}$$

where $t_s = d_{\text{T}}/c_s$ is acoustic time scale for d_{T}-layer. Numbers "1" for β and γ indexes mean that these indexes belong to one-dimensional propagation mode $z \ll R_{\text{L}}$.

When writing (2), we assume that initial amplitude of p_{T} is not too small compared to value of the volume module $B \sim 100$ GPa. Indeed, in the experiments that will be discussed below, minimum values of p_{T} are of the order of 10 GPa or more. Accordingly, rollover and formation of triangular SW occurs at propagation distances comparable to d_{T} scale.

If amplitudes of p_{T} are very small, first, the wave propagates over long distances in linear mode, i.e., without tipping over (respectively, without forming a jump). And, secondly, in terms of amplitude, we begin to get out of plastic approximation. In this case, it is necessary to take into account elastic characteristics of the medium and elastic-plastic effects. Typical values of elasticity thresholds p_{el} for metals are of the order of fractions of GPa [34].

On the diverging section $z > R_{\text{L}}$ we have

$$p \propto p_*(R_{\text{L}}/z)^{\beta_{2.3}} \propto p_*(t_L/t)^{\gamma_{2.3}}, \tag{3}$$

where $t_L \approx R_{\text{L}}/c_s$, β_2 refers to 2D case, and β_3 refers to 3D case; similarly for γ. Pressure $p_* \propto p_{\text{T}}(d_{\text{T}}/R_{\text{L}})^{\beta_1}$ (3) is pressure on the geometry change crossover at $z \approx R_{\text{L}}$.

3. Values of SW attenuation indices

As mentioned above, values of indices (2) and (3) are determined by which region in terms of amplitude and geometry we fall into. Schematically, these areas are presented in table 1.

Dimension of the space is N, where $N = 1, 2, 3$ in plane (1D), cylindrical (2D), and spherical (3D) cases, respectively. There are four indexes α, β, γ, and n.

The index α sets the trajectory of the object: $z \propto t^\alpha$. The indices β and γ are defined by (2) and (3). The n indicator determines how quickly SW weakens as mass of M area behind the SW front increases:

$$p \propto 1/M^n \propto 1/z^{Nn}. \tag{4}$$

3.1. Weak and moderate amplitudes

Consider compressions that are less than B—the average column in table 1. Value B plays the same role as background or undisturbed pressure p_0 in problems of linear and weakly nonlinear acoustics in gases. Thus, gas acoustics is related to acoustics in condensed media.

Table 2. β values in linear case.

$N = 1$	$N = 2$	$N = 3$
0	1/2	1

Gas dynamics equations can be decomposed by perturbation amplitude $p = p_0 + (\delta p)$, where $(\delta p) \ll p_0$. In a cohesive medium (condensed medium), condition of small amplitude has the following form:

$$(\delta p) \ll B. \tag{5}$$

In this case, value of p_0 in condensed phase can be arbitrary, usually $p_0 = 0$. In case of the first order of amplitude (δp) we get wave equation $(\delta p)_{tt} - c_s^2 \, \Delta(\delta p) = 0$. Laplacian Δ is equal to

$$\frac{1}{r^{N-1}} \frac{\partial}{\partial r} \left(r^{N-1} \frac{\partial}{\partial r} \right) \tag{6}$$

for $N = 2$ (cylindrical case) and 3 (spherical case). For $N = 2$, the variable r in (6) is cylindrical radius. In spherical geometry we have

$$\Delta = r^{-1} \partial_r^2 \big(r \, (\delta p) \big). \tag{7}$$

In linear case, $\alpha = 1$, since the wave propagation speed is equal to undisturbed speed of sound. Then indexes in formulas (2), (3) are equal to each other:

$$\beta_i^{\mathrm{lin}} = \gamma_i^{\mathrm{lin}}, \qquad i = 1, 2, 3. \tag{8}$$

Amplitude of the jump decreases in accordance with the index β^{lin}. Index values are shown in table 2. How these values are obtained is described in [48, chapter 8]. In spherical case, this behavior is related to representation of the Laplacian as (7).

The wave produced by heating with ultrashort laser pulse consists of compression section $p > 0$ and stretch section $p < 0$. Now we are talking about wave in 1D geometry—this is curve 1 in figure 1. Appearance of a stretch section is due to the fact that layer of high-pressure stationary matter produces two acoustic waves. The one that runs to border with vacuum changes the sign of pressure (becomes stretching) after reflection from the border.

There is a remarkable fact highlighted in [48, chapter 8]. Linear acoustic wave running from center of symmetry in $N = 2$ or 3 geometry must have a stretch section if compression section extends ahead. This behavior is due to reflection from center of symmetry; not to reflection from boundary with vacuum, as in 1D case.

Moreover, in case of 2D, stretch section does not have last characteristic (as in 1D and 3D)— in 2D, this section continues to the center $r = 0$, see [48, chapter 8]. In our problems, wave passes from flat (curve 1) to radially divergent (curve 2) propagation mode, see figure 1. In this case, part with the stretch is inherited from 1D flow. But spatial divergence at $z_c > R_{\mathrm{L}}$ transforms this part in its own way.

3.2. Weakly linear mode

Linear case is considered in subsection 3.1. Let us proceed to weakly linear case.

A deep study of acoustic problems with weak nonlinearity was performed by L D Landau during the Second World War years [48]. The work was related to the determination of laws of attenuation of hydrocarbons generated by the explosion or flight of a hypersonic vehicle. With weak non-linearity, it is still assumed that $\alpha \approx 1$ and equalities (8) are approximately preserved.

Table 3. β values at weak nonlinearity.

$N = 1$	$N = 2$	$N = 3$
$1/2$	$3/4$	$1 + \varepsilon$

The indexes calculated in the book [48, chapter 10] are shown in table 3. Adding the value ε at $N = 3$ means that the jump amplitude changes according to law $p \propto 1/(z_c \ln(z_c/a))$, where the constant a has length dimension. Recall that in linear case for $N = 3$, attenuation occurs according to law $p \propto 1/z_c$, see table 2.

Comparing tables 2 and 3, we see that due to non-linearity, the attenuation is faster. The β indexes increase by $1/2$, $1/4$, and ε when $N = 1, 2$ and 3, respectively. The increase in indices is caused by the broadening of the triangular area. If the area under the triangular wave is preserved, this broadening leads to a decrease in the amplitude of the jump.

In [48, chapter 10], it is indicated that a structure of two jumps is formed when an acoustic disturbance is emitted from the center of symmetry of a cylinder or sphere. In this case, the first jump is normal. It is formed, as mentioned above, when the compression wave overturns. In fact, the second jump is also natural. The second jump is formed inside the stretch wave. This is due to the difference in the speeds of the characteristic at the maximum $|p < 0|$ of the stretch and the characteristics following it.

There is a focus and intersection of characteristics on the plane z, t. Note that in our problems in flat (1D) geometry, the situation is similar. Because of focusing in two places, a structure of two parts is also formed. In this case, the first line runs before the compression wave, and the second closes the stretch section [50, 51].

3.3. Strong waves

Let us consider the right column of table 1. It corresponds to strong SW, the amplitude of which significantly exceeds the module B, compare with (5). In such a situation, it is not necessary to consider the SW either weakly or moderately nonlinear. At the same time, the speed is $\dot{z}_c$ (see figure 1) significantly exceeds the unperturbed speed of sound. In addition, the Mach number for the speed $\dot{z}_c$ changes with a decrease in the SW amplitude. Accordingly, the relation $\alpha = 1$ and formula (8) are not applicable.

In a highly nonlinear wave, linear acoustics ratio does not work, linking local values of velocity and pressure perturbations via acoustic impedance:

$$p = Zu. \tag{9}$$

Pressure beyond the order of the velocity head

$$p \sim \rho_0 u^2, \qquad u \sim \dot{z}_c. \tag{10}$$

For an approximate description of the situation with a strong SW on the border with vacuum, the classics of natural science developed an approach called in the literature "the short-impact problem" [49]. Here, "short" means that the SW is observed at times that are much longer than the duration of the "impact". The word "impact" is used in the sense that it is strong, distributed in the limit compression mode. In this mode, in ideal gas, the compression is $(\kappa + 1)/(\kappa - 1)$, where κ is the adiabatic index. This approximate description is suitable for case of a strong femtosecond laser pulse—the right column of table 1.

On a short hit, the indexes α, β, γ, n are linked. It is enough to set one of them to determine the rest:

$$\beta = N\,n, \qquad n = 2\frac{1-\alpha}{N\,\alpha}, \qquad \gamma = \alpha\,\beta. \qquad (11)$$

The relations (11) follow from (2), (3), (4), (10), and similarity relations $\dot{z}_c \sim z_c/t$. The short-impact problem is solved in the ideal gas approximation with the adiabata indicator κ. The book [49] shows the results of index calculations of α, β, γ, n (11) in geometry with $N = 1$ for three gas values of the indicator $\kappa = 1.1, 7/5, 5/3$ and one value, corresponding to the condensed phase $\kappa = 2.8$; in this case, the Grüneisen parameter $\Gamma = \kappa - 1$ is close to 2. According to [49] for $N = 1$, $\kappa = 2.8$, the index values α, β, γ, n (11) are equal to

$$\alpha = 0.656, \qquad \beta = 1.045, \qquad \gamma = 0.686, \qquad n = \beta = 1.045. \qquad (12)$$

The interrelation between the problems of a short impact and a strong explosion of Sedov is important. For a short impact, the surface $z = 0$ in figure 1 is a free surface (boundary with vacuum). In a strong explosion, the $z = 0$ boundary is an absolutely rigid plane. Indexes α, β, γ, n in case of a strong explosion are simple (self-similarity of the first kind):

$$\alpha = \frac{2}{2+N}, \qquad \beta = N, \qquad \gamma = \frac{2N}{2+N}, \qquad n = 1. \qquad (13)$$

We remind you that these indexes determine the attenuation of SW during its propagation (2), (3). In (13), the value $N = 1, 2, 3$ is equal to the dimension of the space in which the SW runs. From formulas $\beta = N, n = 1$, it follows that at a fixed time with a strong explosion of pressure of the same order over the entire volume covered by the SW at this time.

Comparing (12) and (13), we see that for $N = 1$ and $\kappa = 2.8$, the solutions for a short strike and a strong explosion are close: the indexes of α differ by 1.6%, $(\frac{2}{3} - 0.656)/(\frac{2}{3}) = 0.016$, the difference between the n indices is 4.5%.

The book [49] presents approximate calculations of the short-stroke problem at $N = 2$ and 3. The following follows:

- The solutions to the problems of short impact and strong explosion in a condensed medium $\Gamma \approx 2$ differ little for all three values of N. With a short impact, the SW attenuates only slightly faster than with a strong explosion.

- Only a small fraction (percent) of the mass covered by the SW flies out of the plane $z = 0$ in figure 1—therefore, the mass of the laser torch is small.

- At long times, the distance z_c is significantly greater than the distance w to the center on the plane $z = 0$ in figure 1.

- The flow is rotated at a distance of $z_{\mathrm{revrs}} \approx 0.5z_c$ from the point z_c vertically $x = 0, y = 0$ in case of $N = 1$ in figure 1. At the point of rotation, the z component of the velocity changes its sign: at the segment $z_c < z < z_{\mathrm{revrs}}$, this component is directed towards the SW, and at $z > z_{\mathrm{revrs}}$—towards vacuum. For $N = 2$ and 3, the point z_{revrs} in figure 1 is located below $(z_{\mathrm{ret}} \approx (0.7\text{–}0.8)r_c)$, than in case of $N = 1$.

Degrees of β in the short-stroke problem (see right column of table 1) are shown in table 4. Comparing table 4 with table 3, we see that strong nonlinearity significantly increases the rate of SW attenuation. In Sedov case (13) we have $\beta = N$.

4. Experimental situation

The research presented in this paper is conducted in the interests of studying the physics of laser hardening of metals. Different laser systems are used to generate laser shock waves. Their main difference is the duration of the pulse τ_{L}. In addition, the energy of the impact is important. Our work deals with ultrashort laser pulses. The term "ultrashort" means that the duration of

Table 4. β indexes in condensed matter with strong nonlinearity.

$N = 1$	$N = 2$	$N = 3$
≈ 1.045	≈ 2.1	≈ 3.2

the laser pulse τ_{L} is less than the acoustic time scale. This scale is equal to $t_s = d_{\mathrm{T}}/c_s$, where d_{T} is the thickness of the warmed up layer, c_s is the speed of sound.

Calculations of the action of a nanosecond laser pulse are described in the works [20, 52, 53]; previous literature is also discussed there.

The pressure created by the laser pulse varies over time from the maximum value to small values related to pressure before the laser action begins. The maximum pressures in case of an ultrashort pulse are much higher than those that occur during nanosecond impacts at comparable absorbed energies F_{abs}. When the intensity absorbed by the target is of the order of 1 GW/cm^2 maximum pressure for nanosecond exposure in water of the order of 1 GPa [20, 52, 53].

In this paper, we consider the pressure fields created by an ultrashort pulse, since it is with high pressures that the processes of forceful change in the grain structure of a polycrystalline target material—the grinding of crystallites—are associated.

In the case of an ultra-short pulse, there is no need to use a layer of water to amplify the mechanical pulse transmitted to the target. New femtosecond laser hardening technologies [4, 6] are associated with understanding this circumstance. Accordingly, there are no very significant restrictions on the energy of laser exposure due to nonlinear processes in the liquid and with optical breakdown of the liquid [20, 54, 55].

Power and energy are widely spread femtosecond laser systems are the units of millijoules, respectively, dozens of gigawatt. Therefore, when focusing into a spot with a diameter of 50 μm, the incident fluence F_{inc} is easily adjusted to the values $\sim$ 10–100 J/cm^2. When focusing into a spot with a diameter of 5 μm, the values of F_{inc} increase by two more orders of magnitude.

We will focus on experiments [56, 57], in which the laser pulse energy was of the order of a microjoule. In this case, the irradiation spots were near the diffraction limit of focus, i.e., they were several microns. Then the falling fluence F_{inc} reached values of the order of 10 J/cm^2.

For our calculations, the values of the absorbed fluence are important $F_{\mathrm{abs}} = (1 - R)F_{\mathrm{inc}} = AF_{\mathrm{inc}}$, where R and A are the reflection and absorption coefficients. The coefficient A depends on the metal and the wavelength of the incident radiation. There are cases with high and moderate reflection coefficients. With a good reflection, the A coefficient is of the order of percent. When using the second harmonics of systems on titanium-sapphire, chrome-fosterite, or when using the second harmonic of the ytterbium fiber laser [57], the a coefficient takes moderate values of the order of 0.2–0.7, even in case of well-reflecting metals. The values of the coefficients R and A in linear modes of interaction of a monochromatic electromagnetic wave with a substance were discussed above. These values for a clean, well-polished surface are given in [58–60].

In the case of fs pulses with the energy we are considering, a strong heating of the electronic subsystem occurs. As a result, the values of R change [61]. These changes are especially significant in case of high values of the reflection coefficient R.

Indeed, the effects (heating, pressure amplitude) are related to the absorbed energy. And this energy varies from a value of the order of 0.01 from the incident energy to a value ten times greater when the electronic subsystem is strongly excited. Curiously, in case when the coefficient A is not small, say $A \approx 0.5$, the coefficient A even decreases slightly when the electronic subsystem is excited. However, this effect does not play the decisive role as in case of well-reflecting metals.

So, we will focus on the laser pulse energy of the order of microjoules, the spot diameters of the order of 3–6 μm, and the incident energy in the tens of J/cm^2. The other typical parameters are: the second harmonic of the laser radiation, the coefficient A of the order of 0.3. Then the maximum absorbed energy will be of the order of units of J/cm^2. For gold with a characteristic warm-up depth of a femtosecond pulse $d_T \sim 100$ nm, the absorption of this amount of energy creates maximum pressures of several Mbar.

5. Initial conditions and geometry of hydrodynamic calculation

As mentioned above, ultrashort laser action creates a surface heating layer with a thickness of d_T for the duration of the pulse τ_L, which is small compared to the hydrodynamic time $t_s = d_T/c_s$. On the time scale $\sim t_s$, the hydrodynamic effects associated with the decay of the high-pressure d_T-layer into acoustic waves and entropy-vortex mode become decisive.

It is clear that in hydrodynamic numerical modeling, it is acceptable to consider the Cauchy problem with initial data instead of the laser heating stage. In this case, we compress the time interval τ_L to zero and start our numerical calculation directly from the heating zone created at the end of the laser pulse. The heating zone is a layer in which the temperature and pressure are sharply increased compared to their values before the start of the laser pulse.

Exclude from the analysis a thin layer at the boundary with vacuum in which the significant effects of electronic pressure p_e. This layer thickness of $c_s t_{eq}$, since pressure p_e exceeds pressure of the ion subsystem over times of the order of time of existence t_{eq} of the surface of two-temperature (2T) state [62–68].

Note that the model [69–71] does not take into account the effect of electronic pressure. It is a hybrid model in which 2T physics is embedded in molecular dynamics (TTM+MD).

For gold, the 2T relaxation time is 3–6 ps; the thickness of the electron rarefaction wave is $c_s t_{eq} \approx 12$ nm, respectively. The warm-up zone is $d_T \approx$ 100–150 nm. For other metals, the values t_{eq}, $c_s t_{eq}$, d_T are significantly less. But the ratio $c_s t_{eq} < d_T$ is preserved.

In our formulation of the hydrodynamic problem, the emphasis is on non-one-dimensional effects. The one-dimensional situation is studied in detail, see, for example, [62–65, 70, 71]. But as mentioned above, the applicability of the one-dimensional calculation is limited in time by the second acoustic scale; the first scale is $t_s = d_T/c_s$, the second scale is determined by the spot radius $t_{geom} = R_L/c_s$. The restriction on the distance of passage into the target thickness is due to the radius R_L, see figure 2.

In experiments, the laser beam passes through vacuum and is absorbed into a gold target, see figure 3. Fast (supersonic [64, 72, 73]) heating due to the dramatically increased electronic thermal conductivity in 2T conditions [64, 72] creates a heating d_T-layer. Formation of the d_T-layer occurs at the 2T-stage.

Further in time, this layer expands very slowly (compared to sound and even hydrodynamic speeds): the heat transfer goes into subsonic mode of electronic heat wave propagation [64,72,73].

There are two defining geometric parameters of the problem. First, this is the thickness of the warmed up d_T-layer, see figure 3. Second, it is the size of the lighting spot R_L, these parameters are shown in figure 3. We believe that the intensity distribution across the spot is constant. Outside the spot, the laser beam intensity is zero. That is, the intensity distribution is similar to the shape of a flat-topped hat.

We are interested in the transition from a one-dimensional to a non-one-dimensional mode of acoustic perturbation propagation. This transition is performed at propagation distances of the order of the spot radius R_L. In typical experiments, the radius R_L is much greater than the thickness of the warmed up layer $d_T \sim 0.1$ μm. This is true even when focusing at the diffraction limit, when $R_L \sim \lambda \sim 1$ μm for the optical range of electromagnetic wavelengths. Since $R_L \gg d_T$, then pressure distribution profile along the y coordinate at an early stage inside the heating d_T-layer has a weak effect on the acoustic wave profile at distances of the order
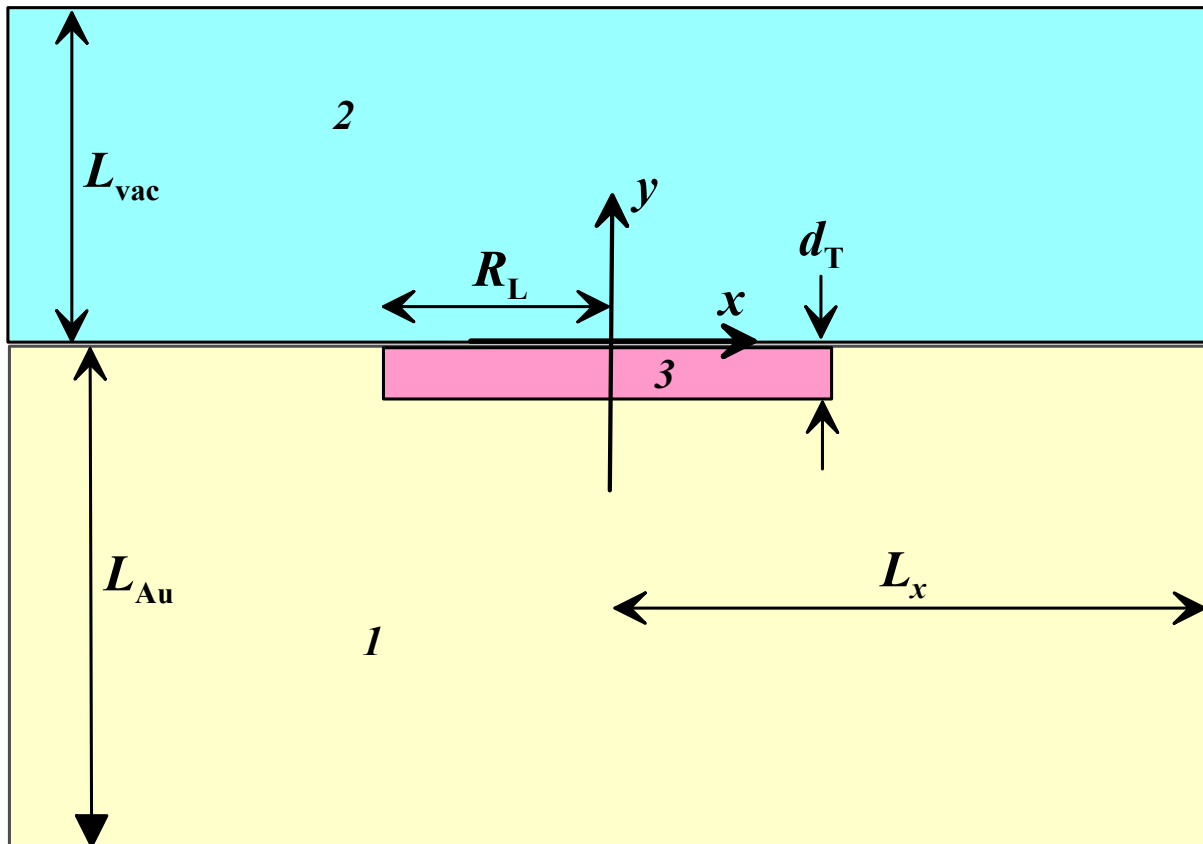
Figure 3. Diagram of the effect of an ultra-short laser pulse on the volumetric target (*1*). The half-width laser beam R_L passes through vacuum (*2*) and acts on the target. Ultrashort beam action in a hydrodynamic setting "instantly" creates a warmed up layer *3* with a thickness of d_T. The lengths of L_x and $L_{Au} + L_{vac}$ determine the size of the calculated box.

R_L. Therefore, our calculations assume that the temperature and pressure distribution inside rectangle 3 in figure 3 is uniform in space. The density inside rectangle 3 is uniform at the initial moment of time, since $\tau_L \ll t_s$, and the rectangle with sides d_T and $2R_L$ does not have time to unload in the vacuum direction. In addition, as mentioned above, we neglect unloading in the electronic vacuum wave.

There are three statements of the problem taking into account the spatial geometry:

(i) Illumination of the target with a cylindrical lens. The movement occurs in the plane of figure 3 along the coordinates y (normal) and x (tangential direction)—2D geometry.

(ii) Spherical lens that acts as a normal to the target. The flow is axially symmetrical. Current lines are located in planes that pass through the lens axis. The motion can be described both in full 3D geometry and in geometry associated with the cylindrical radius r_{cyl} and the coordinate z along the lens axis and along the normal to the target plane.

(iii) Spherical lens that illuminates the target at an angle. In this case, the lighting spot is an ellipse. The problem is solved in 3D geometry with coordinates z, x, y.

In this paper, we will limit ourselves to case i. Cases ii and iii require separate consideration. The geometry and coordinate system corresponding to case i are shown in figure 3. The calculation is performed in a rectangular calculation area with the dimensions of the rectangle L_x horizontally in figure 3 and $L_{Au} + L_{vac}$ horizontally. To save the calculated cells, the symmetric

half of the flow is used at $x > 0$. Free boundary conditions are set on the upper, right, and lower boundaries of the calculation area. On the left border of the rectangle $x > 0$ (the y axis in figure 3) the symmetry condition is applied.

An important parameter is the ratio R_L/d_T of sizes of rectangle 3 in figure 3. The ratio of pressures depends on this ratio: the ratio of the initial pressure in rectangle 3 to pressure at the stage of the flow adjustment from quasi-one-dimensional to quasi-cylindrical; here we mean a cylinder with a guide along the z axis in figure 3; the z axis is perpendicular to the plane of figure 3.

So, the situation at the ends of the time interval covering the quasi-one-dimensional stage of the flow depends on the value of R_L/d_T. Whereas how long our tracking of the quasi-cylindrical stage is depends on the ratio of lengths L_x/R_L, r_{Au}/R_L. It is clear that it is desirable to have the largest possible values of these relations in order to determine the asymptotic attenuation of the diverging quasi-cylindrical shock wave. Of course, the values of the relations L_x/R_L, R_{Au}/R_L are limited by computer resources: limits on memory and duration of the simulation. While the need to allow the heating d_T-layer determines the maximum size of the calculated cell $\Delta x = \Delta y$.

We use Eulerian hydrodynamic code: a structured rectangular uniform grid covers a rectangle with sides L_x and $L_{Au} + L_{vac}$. The code passes through the contact boundaries in an end-to-end way. The most important is the contact between target substance 1 (gold) and "vacuum" 2; 1 and 2 are the area numbers in figure 3. In our code, we cannot lower "vacuum" density to zero. We will present two calculations below. In the first one, the density of a substance in vacuum is equal to 200 kg/m³. In the second calculation, "vacuum" density is 2 kg/m³. Accordingly, the ratio of gold ($\rho_0 = 19\,300$ kg/m³) and vacuum densities equals $1/97$ and 10^{-4}, consequently, in these two cases.

In the future, a separate calculation will be performed with the density of medium in area 2 in figure 3 is equal to 1000 kg/m³. This is necessary to describe the non-dimensional propagation of a laser shock wave in water when exposed to gold through water [16, 19, 20, 52, 74, 75]. This problem is interesting in connection with applications that study the synthesis of nanoparticles during ablation into a liquid.

6. Approximation of the equation of state

As mentioned above, the Euler hydrodynamic code used describes the contact boundaries in an end-to-end way; that is, contacts between substances are not tracked-there is a noticeable numerical diffusion that smears the boundary. Therefore, to use the Euler code, you need cross-cutting equation of state, which describes the cold gold in region 1 in figure 3, hot gold under high pressure in area 3 and vacuum 2. Pressure in region 3 rises due to strong isochoric (i.e., at constant density) heating.

As such, we will use "shifted" equation of state of ideal gas. Let us explain what this means.

The most important circumstance that distinguishes the EOS of a condensed substance is the ability of such a substance to resist stretching (negative pressures) and the ability to maintain the final density ρ_0 at zero pressure.

Of course, this circumstance is due to the cohesive component (attraction of atoms) in the potential of interatomic interaction. In addition, it is known that condensed substances are rigid, they have a sufficiently large Grüneisen parameter Γ. This parameter determines the value of the thermal contribution to pressure $p_T = \Gamma e$, where e is the thermal addition to the energy.

In case of gas, the interaction potential has a small cor (interaction radius). The size of the crust is small compared to the interatomic distance. Potential energy can be neglected in comparison with the kinetic energy of atoms. In case of gas, the adiabatic index $\gamma = \Gamma + 1$ replaces the Grüneisen parameter. In gas, $p = nk_B T$, $e = (N/2)nk_B T$, where e is the kinetic (thermal) energy of gas per unit volume, N is the number of degrees of freedom of an atom or molecule, $\gamma = (N + 2)/N$, n is the concentration of atoms or molecules, k_B is the Boltzmann
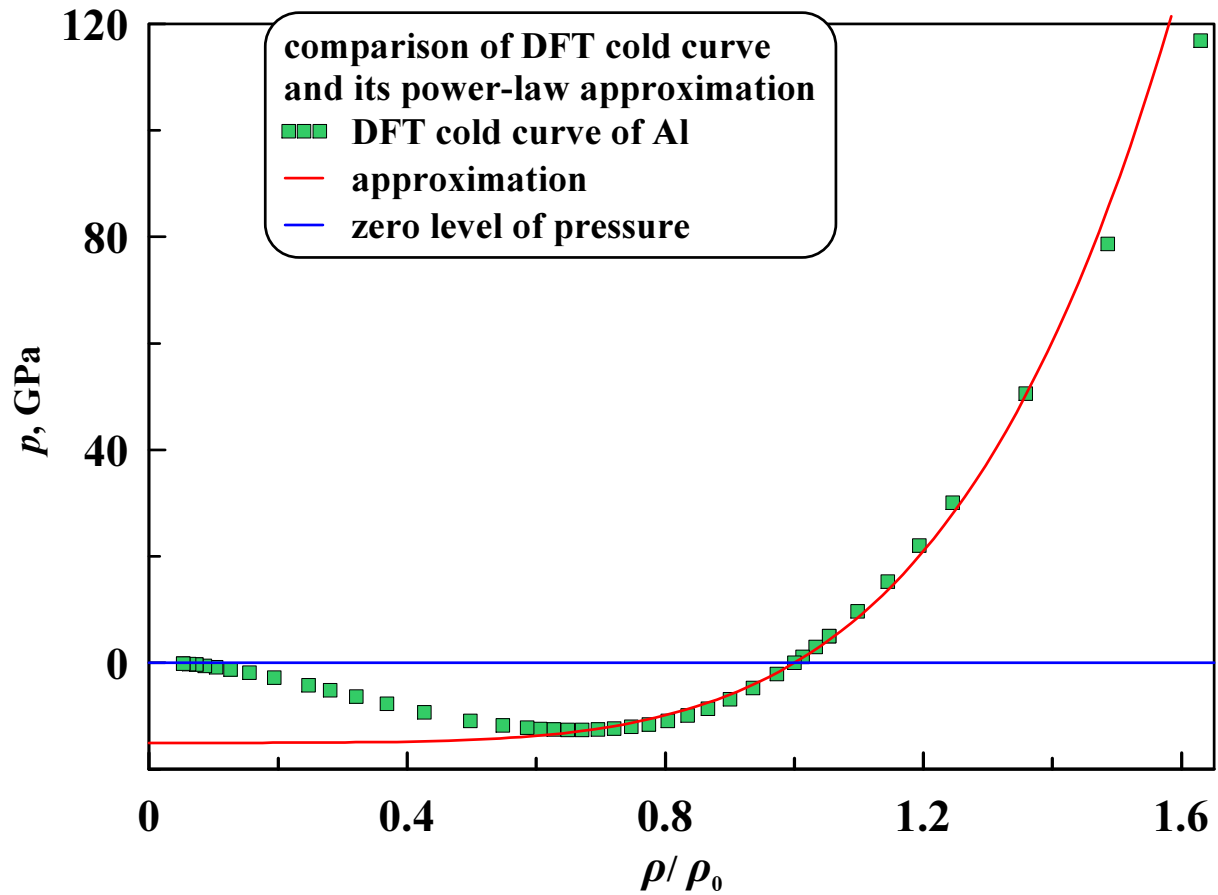
Figure 4. Equation of state of the target substance and approximation of this equation.

constant. Hence the ratio $\gamma = \Gamma + 1$. We see that in case of gas, pressure $p = 0$ is only reached at zero density: $n = 0$.

In order to use equation of state of ideal gas, but at the same time avoid the condition $p = 0$ at $n = 0$, we need the above-mentioned "shift" in pressure. To achieve this shift, we use buffer gas that fills "vacuum" 2 in figure 3. The condensed medium that our equation of state approximates is aluminum. This material often serves as a target in ablation experiments in air and liquid.

Figure 4 shows the cold curve (green markers) and its approximation (red solid curve). As approximating equation of state, we use ideal gas. Two parameters, namely pressure shift p_{bg} and adiabatic index γ can be varied to find the best approximation. Adiabatic equation of such gas is

$$p = p_0(s) \left(\rho / \rho_0 \right)^{\gamma} - p_{\text{bg}}. \tag{14}$$

The best approximation of the cold curve in figure 4 is achieved with a degree of $\gamma = 4.8$ and a background pressure of $p_{\text{bg}} = 15$ GPa. The approximation covers pressure range up to Mbar values of interest, see the end of section 4. Curve (14) is shifted down pressure by subtracting the constant p_{bg}. This technique takes into account the negative pressure zone that occurs when the condensed medium is stretched.

The calculations use equation of state (14) without a shift in pressure. In the state before the impact of the laser pulse, the system from target 1 and vacuum 2 in figure 3 is in force balance. In this case, pressure distribution is uniform across the entire calculation area and is

equal to the background value p_{bg}. This is achieved, first, due to the small but finite density of gas in "vacuum" 2 in figure 3. Second, we strongly heat vacuum gas so that its pressure is equal to the value of p_{bg}, as in the target, at a much lower density. Thus, the extension of target 1 in figure 3 of gas is forcibly balanced by the back pressure of the buffer, which is "vacuum" in region 2 in figure 3.

In case of vacuum, pressure equal to zero is always maintained at the boundary of condensed medium with vacuum. The corresponding boundary condition is called a free boundary condition. In terms of the dynamics of a condensed medium, it is important not that the pressure at free boundary is zero, but that pressure at boundary of a dense substance does not change over time and is always uniform along the boundary. In our situation with buffer gas 2 in figure 3 we are approaching a free boundary configuration using very low density buffer gas.

The pressure equilibrium gives $n_{\mathrm{vac}}T_{\mathrm{vac}} = n_t T_t$, where n_{vac}, T_{vac} and n_t, T_t is the density and temperature of vacuum and the target, respectively. The ratio of the acoustic impedances of the target and vacuum is equal to

$$z_t/z_{\mathrm{vac}} = (n_t \sqrt{T_t})/(n_{\mathrm{vac}} \sqrt{T_{\mathrm{vac}}}) = \sqrt{T_{\mathrm{vac}}}/\sqrt{T_t}. \tag{15}$$

As you can see, in a hot, low-density vacuum, this ratio is high. Hence, the buffer vacuum in region 2 in figure 3 is indeed dynamically equivalent to vacuum in relation to a dense, relatively cold target 1 in figure 3.

As mentioned above, we are interested in the hydrodynamic stage of development of processes caused by ultra-short laser exposure. At this stage, the effects of thermal conductivity become insignificant, since the coefficient of thermal conductivity at the single-temperature (1T) stage is reduced to tabular values. Accordingly, the speed of thermal conductivity heat transfer becomes less than the speed of sound and hydrodynamic speeds. This circumstance allows us to ignore the thermal conductivity in our hydrodynamic calculations, although there are large temperature contrasts.

Thermal conductivity becomes important again in the later stages. At these stages, the melt recrystallization occurs. Here we will limit ourselves to the hydrodynamic stages, which are completed before recrystallization.

7. Calculation results: Shock wave geometry

Figures 5 and 6 illustrate, in particular, the effect of the ratio of densities of vacuum and target on the results. Unloading the hot rectangle 3 in figure 3 in the direction of vacuum induces the appearance of a shock wave in vacuum. The speed of sound in very hot vacuum is high. Therefore, the vacuum shock wave quickly runs through the vacuum in rectangle 3 in figure 3 and goes through the boundary conditions of free flow on the upper and right side borders of rectangle 2. In this case, there is an action of a shock wave in vacuum on the target through the boundary of the target with vacuum.

The shock wave in vacuum runs fast. It overtakes the shock wave in the target. This is clearly seen in figure 5. At the time of 100 ps, the shock wave in the target, running along the border with vacuum, passed a path of about 500 nm. While the shock wave in vacuum has already left the vacuum rectangle. The shock wave in vacuum imprinted a trace in the target—this is an oblique weak shock wave. The oblique wave is located at distances along the x axis from 500 to 1000 nm near the boundary of the target with vacuum (below the horizontal $y = 0$). It corresponds to a faint trace of bluish-bluish color in figure 5. This trace is weak, since the ratio of densities of 1% is small; this was the ratio in case of the calculation shown in figure 5. When the density ratio decreases to 10^{-4}, the trace of the vacuum shock wave becomes so weak that it cannot be seen in figure 6.

The development of the shock wave generation and propagation process in the target is shown in figure 7, 8, and 6. These figures refer to time points 10, 30 and 100 ps, respectively. If at time
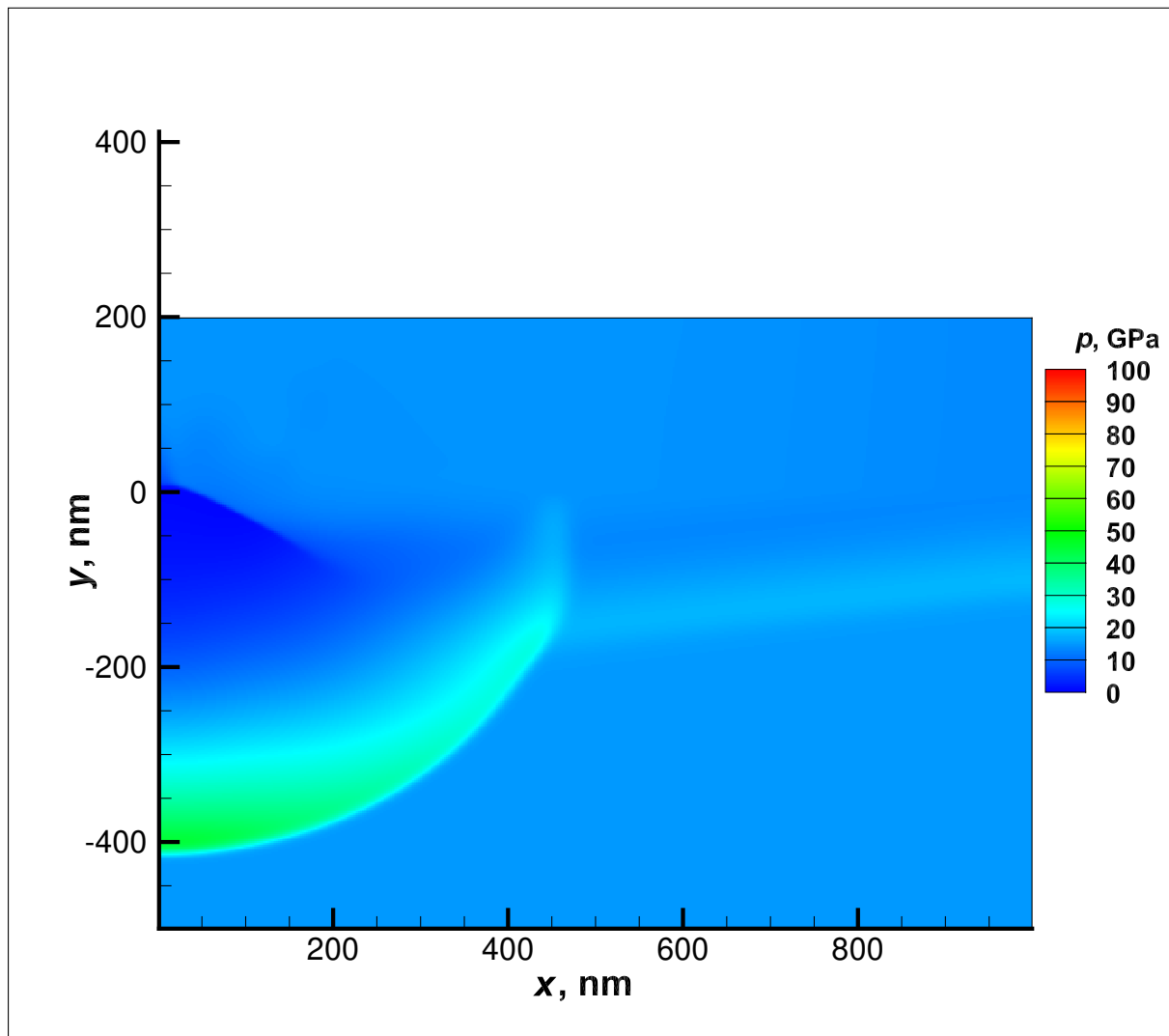
Figure 5. Two-dimensional hydrodynamic calculation in the coordinates x, y, shown in figure 3. The geometric dimensions are $d_{\mathrm{T}} = 50$ nm, $R_{\mathrm{L}} = 200$ nm. The dimensions of the calculated rectangle and the relationship between the height of the vacuum rectangle and the target rectangle are clear from the drawing. A time point of 100 ps is shown. Grid cell size equals 2 nm. At this point in time, the "nose" of the shock wave c (see figure 1) moves away from the boundary with vacuum at distance that exceeds the half-width of the laser beam R_{L}. I.e., the transition from the quasi-flat mode of shock wave propagation to the quasi-cylindrical mode begins. The initial ratio of vacuum and target densities in this calculation is 10^{-2}.

moments of 10 and 30 ps, the current can still be attributed to a quasi-flat flow, figure 6 with $t = 100$ ps clearly refers to the beginning of the quasi-cylindrical stage. Unfortunately, at the moment, our numerical resources do not allow us to track the evolution of the shock wave flow at a distant quasi-cylindrical stage. This is a matter of the next stages of modeling. After the transition from a quasi-flat to a quasi-cylindrical mode, the shock wave attenuation increases.

At the time of 100 ps, force field in figures 5 and 6 still far exceeds the thresholds of elastic-plastic transformations. These thresholds are usually of the order of fractions of 1 GPa, although they can increase by an order of magnitude in ultra-short exposure [36–38,73,76–87]. Therefore,
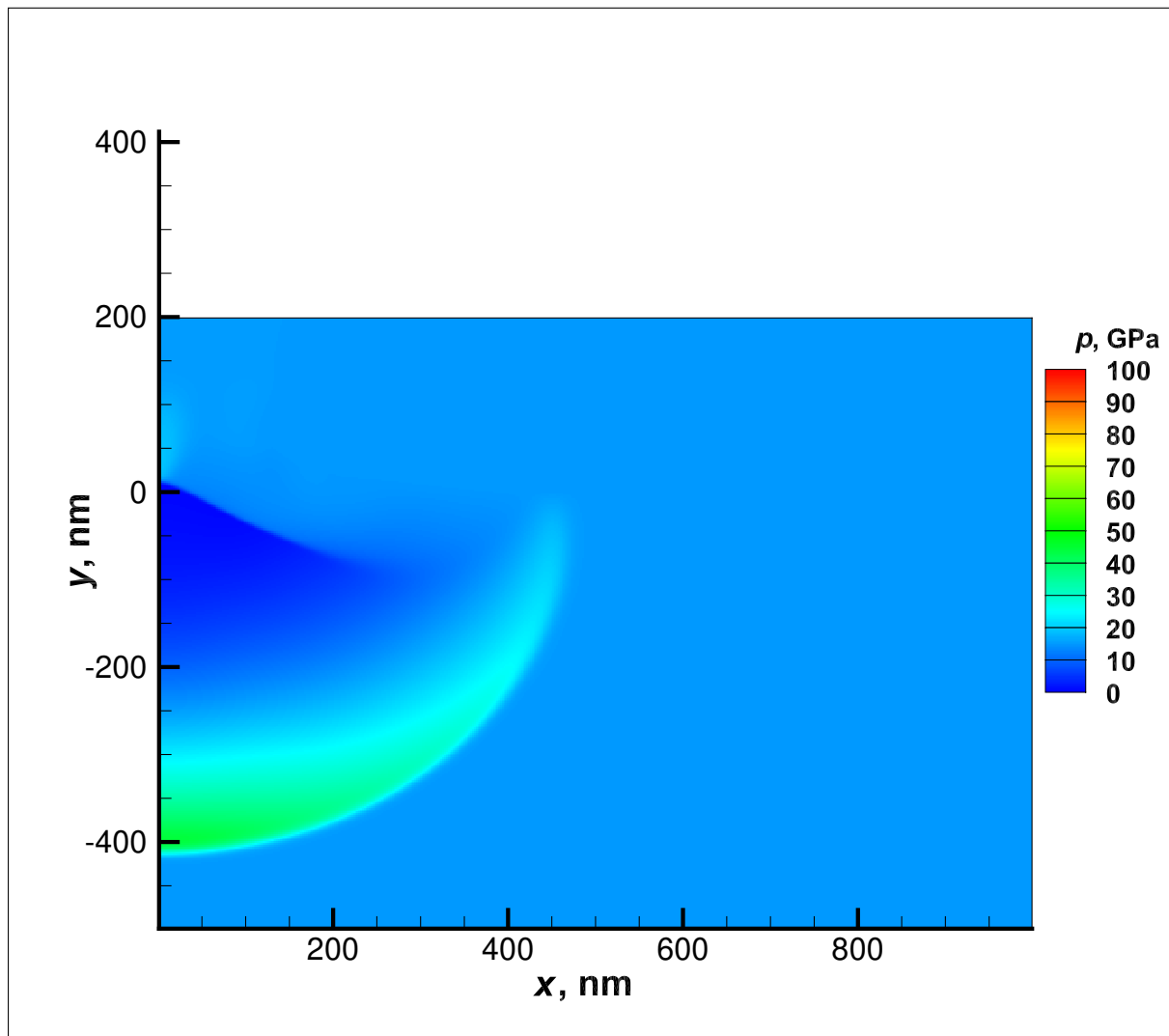
Figure 6. Pressure field at the same time instant $t = 100$ ps as in figure 5. Grid cell size equals 2 nm. This calculation has an important difference from the calculation in figure 5. The ratio of densities between vacuum and target substances has been increased a hundred times. Here it is equal to 10^{-4}. The results differ little. The only noticeable difference is the disappearance of the weak oblique shock wave, which is visible in figure 5.

the flow behind the shock wave at the time instant of 100 ps remains plastic. A simple practical recommendation for using femtosecond pulses to harden metals is as follows. The laser spot must be large in diameter. Then the shock wave attenuation is reduced due to lateral offloads. Accordingly, the shock wave remains strong longer, able to plastically modify the material.

The reddish-yellow areas in figures 5–9 refer to the compressed material. The blue background around the traffic zone refers to the background pressure of 15 GPa, see figure 4 and equation (14). The blue areas on the pressure maps in figures 5–8 represent the areas of tension of the target substance. In them, the pressure drops below the value of 15 GPa. Our calculations do not take into account spillover phenomena. Our calculations confidently represent what happens during compression and moderate stretches. The regions associated with the high-entropy substance of rectangle 3 in figure 3, experience strong stretches to fairly small densities.
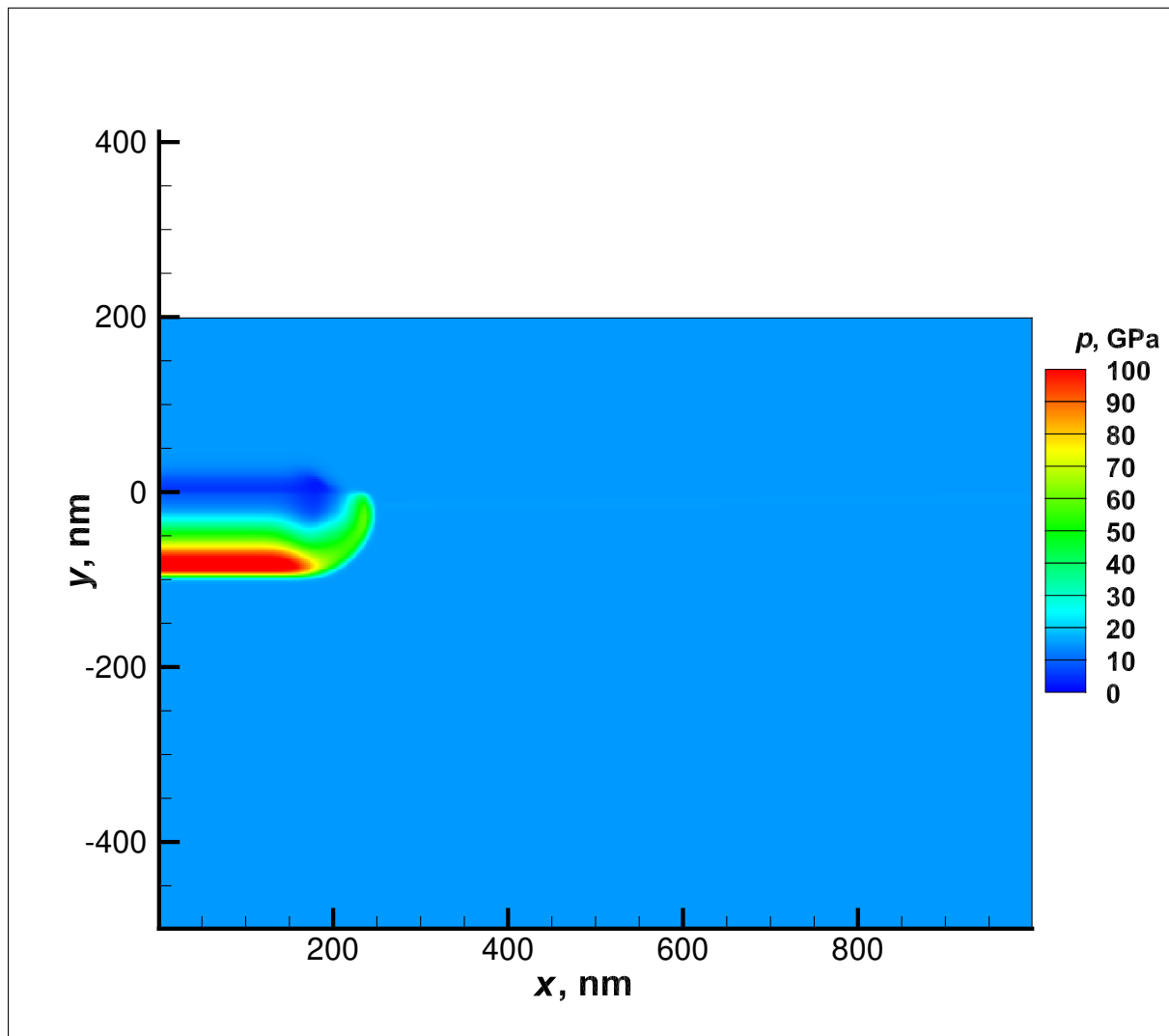
Figure 7. Pressure field of laser-induced flow in a volume target at the instant of 10 ps after a laser strike. Grid cell size is equal to 2 nm. The initial pressure in the rapid heating rectangle 3 in figure 3 was 2.6 Mbar. The ratio of vacuum densities to the target is 10^{-4}. Therefore, acoustic disturbances in vacuum have such a negligible amplitude that they are not visible on this pressure map, compare. with a weak oblique wave visible in figure 5 with a density ratio of 10^{-2}. Ahead, a quasi-flat shock wave runs into the thickness of the target. There are rounding side waves. The blue area refers to the discharge of the heated target material from rectangle 3 in figure 3 in the direction of vacuum.

As mentioned, initial area 3 in figure 3 decays into acoustic perturbations and entropy-vortex mode. Acoustic waves in the order of $t_s = d_T/c_s$ leave the hot rectangle 3 in figure 3. The entropy-vortex mode is associated with the substance of rectangle 3. In the accepted approximation (14) regions of small densities of the entropy-vortex mode (laser torch) are described at a qualitative level. Nevertheless, you can rely on the conclusion about the localization of the fashion in a spot with a diameter of $2R_L$. Figure 9 with a complex structure of the edges of the torch suggests hydrodynamic mechanisms for formation of rollers around laser craters.
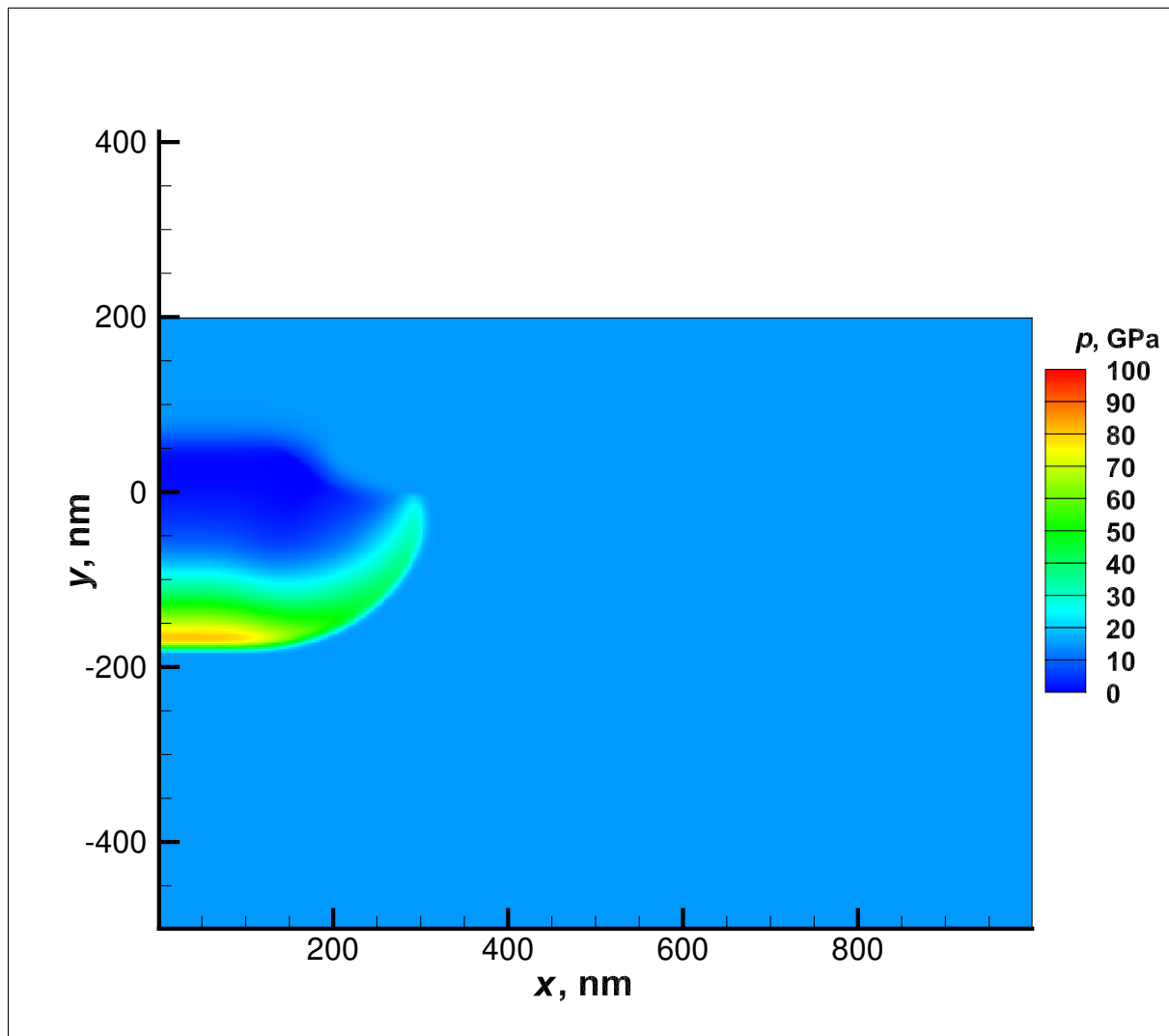
Figure 8. Pressure field at $t = 30$ ps. Grid cell size is 2 nm. The plane shock wave continues to propagate into the target thickness, compare with the situation at the time of 10 ps in figure 7. At the same time, lateral discharge waves are moving further along the front of the flat shock wave. We note a fairly strict limitation of the emission into vacuum (laser torch) by the size of the half-width of the laser beam $R_L = 200$ nm.

Rollers are formed where the melt from the target substance borders on the solid phase. Of said relative binding entropy-vortex fashion to the hot stuff and little influence of heat conduction on the propagation of heat in hand for spots more micron [88], it follows that a cushion is formed at the boundary of liquid and solid phases.
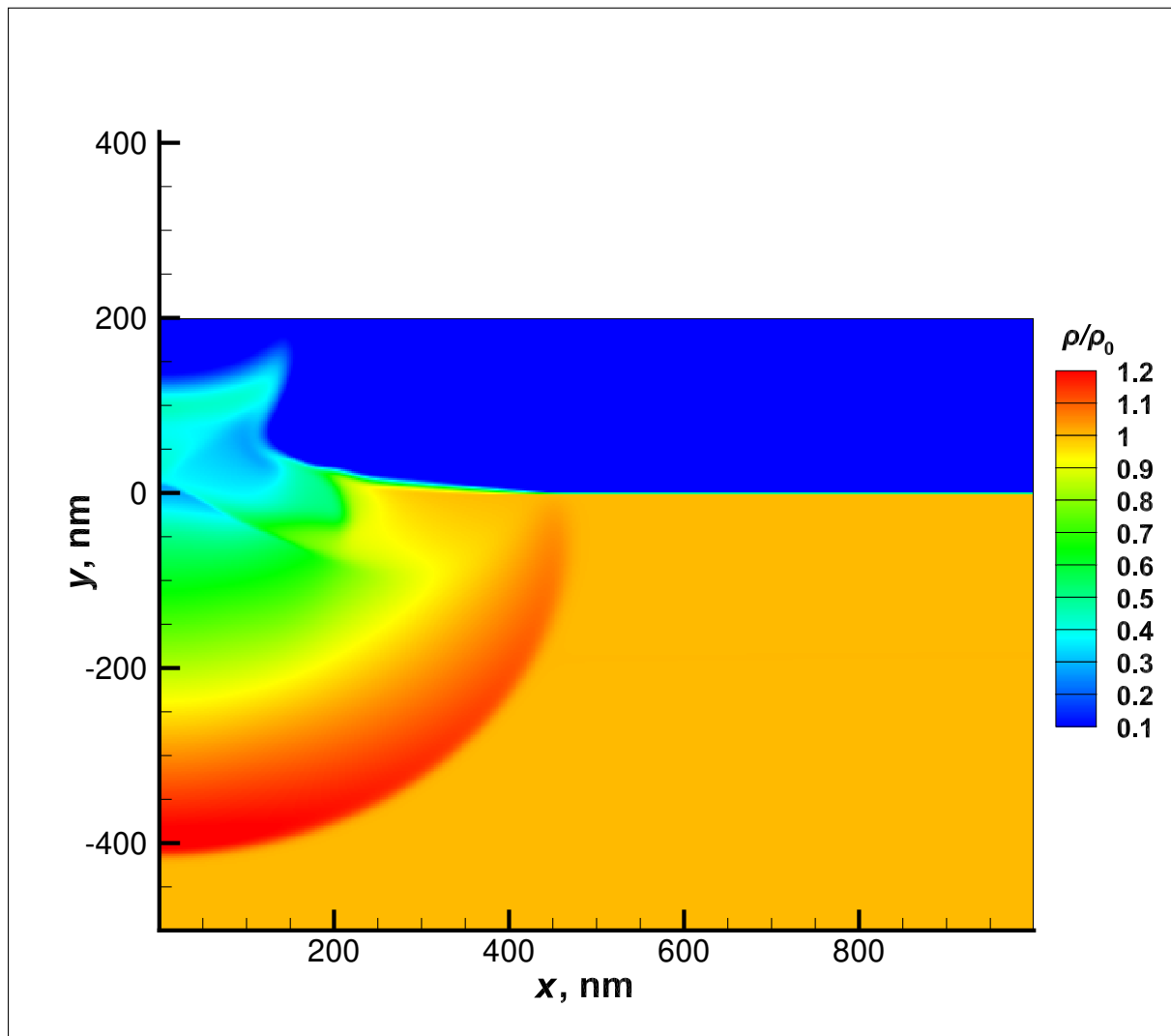
Figure 9. Density field at time 100 ps; density ratio 10^{-4} on square grid. The pressure field at this time for two different ratios of vacuum and target densities was shown above in figures 5 and 6. The structure of the shock-compressed region, the stretch wave, and the laser torch is clearly visible. We see a side wave running along the surface of the target. At our amplitudes, the side wave must be observed in experiments.

8. Conclusion

The paper investigates non-one-dimensional effects, accompanying the propagation of laser shock waves from radiation spots of finite dimensions. These effects are important for applications related to laser hardening of materials (such as laser shock peening) and with the synthesis of nanoparticles during laser ablation in liquid. Geometric effects that determine the depth of transformation of the polycrystalline substance of the target are studied under the action of the stress field behind the shock wave. It is shown that when propagating to a depth of the order of the spot size, the amplitude of the shock wave still significantly exceeds the thresholds of elastic-plastic transformations. Moreover, this result applies to laser systems with conventional energy. It is recommended to use the largest possible femtosecond irradiation spots. Then the effects of lateral shock wave attenuation are reduced and the wave is less attenuated.

Acknowledgments

References

[1] Liao Y, Ye C and Cheng G J 2016 *Opt. Laser Technol.* **78** 15–24
[2] Hoffman J, Chrzanowska J, Moscicki T, Radziejewska J, Stobinski L and Szymanski Z 2017 *Appl. Surf. Sci.* **417** 130–5
[3] Walsh N, Costello J T and Kelly T J 2017 *Appl. Phys.* B **123** 179
[4] Trdan U, Sano T, Klobcar D, Sano Y, Grum J and Sturm R 2018 *Corros. Sci.* **143** 46–55
[5] Inogamov N, Zhakhovsky V, Ilnitsky D and Khokhlov V 2019 Picosecond-nanosecond laser flash, formation of powerful elastic waves in crystals, and shock peening *Proc. of the 32nd Int. Symp. on Shock Waves (ISSW32)* pp 3077–106
[6] Kawashima T, Sano T, Hirose A, Tsutsumi S, Masaki K, Arakawa K and Hori H 2018 *J. Mater. Process. Technol.* **262** 111–22
[7] Stratakis E, Barberoglou M, Fotakis C, Viau G, Garcia C and Shafeev G A 2009 *Opt. Express* **17** 12650–9
[8] Maciulevicius M, Vinciunas A, Brikas M, Butsen A, Tarasenka N, Tarasenko N and Raciukaitis G 2013 *Phys. Procedia* **41** 531–8
[9] Povarnitsyn M E and Itina T 2014 *Appl. Phys.* A **117** 175–8
[10] Zhang D, Gokce B and Barcikowski S 2017 *Chem. Rev.* **117** 3990–4103
[11] Xiao J, Liu P, Wang C and Yang G 2017 *Prog. Mater. Sci.* **87** 140–220
[12] Veiko V P, Volkov S A, Zakoldaev R A, Sergeev M M, Samokhvalov A A, Kostyuk G K and Milyaev K A 2017 *Quantum Electron.* **47** 842–8
[13] Barmina E V, Sukhov I A, Viau G and Shafeev G A 2017 *ChemPhysChem* **18** 1069–73
[14] Mariella R, Rubenchik A, Fong E, Norton M, Hollingsworth W, Clarkson J, Johnsen H and Osborn D L 2017 *J. Appl. Phys.* **122** 075104
[15] Amendola V, Scaramuzza S, Carraro F and Cattaruzza E 2017 *J. Colloid Interface Sci.* **489** 18–27
[16] Inogamov N A, Zhakhovskii V V and Khokhlov V A 2018 *J. Exp. Theor. Phys.* **127** 79–106
[17] Zhang Z, Nian Q, Doumanidis C C and Liao Y 2018 *J. Appl. Phys.* **123** 054901
[18] Kudryashov S I, Saraeva I N, Lednev V N, Pershin S M, Rudenko A A and Ionin A A 2018 *Appl. Phys. Lett.* **112** 203101
[19] Shih C Y, Streubel R, Heberle J, Letzel A, Shugaev M V, Wu C, Schmidt M, Gokce B, Barcikowski S and Zhigilei L V 2018 *Nanoscale* **10** 6900–10
[20] Petrov Y, Khokhlov V, Zhakhovsky V and Inogamov N 2019 *Appl. Surf. Sci.* **492** 285–97
[21] Kudryashov S I, Samokhvalov A A, Nastulyavichus A A, Saraeva I N, Mikhailovskii V Y, Ionin A A and Veiko V P 2019 *Materials* **12** 562
[22] Inogamov N A, Khokhlov V A, Petrov Yu V and Zhakhovsky V V 2019 arXiv:1910.08924v1 [physics.comp-ph]
[23] Leung C L A, Marussi S, Atwood R C, Towrie M, Withers P J and Lee P D 2018 *Nat. Commun.* **9** 1355
[24] Bertoli U S, MacDonald B E and Schoenung J M 2019 *Mater. Sci. Eng.: A* **739** 109–17
[25] Vorobyev A Ya and Guo C 2006 *Opt. Express* **14** 2164–9
[26] Vorobyev A Ya and Guo C 2008 *Appl. Phys. Lett.* **92** 041914
[27] Zhakhovskii V V, Inogamov N A and Nishihara K 2008 *JETP Lett.* **87** 423–7
[28] Inogamov N A *et al* 2014 *J. Phys.: Conf. Ser.* **510** 012041
[29] Inogamov N A *et al* 2015 *Eng. Failure Anal.* **47** 328–37
[30] Bonse J, Kruger J, Hohm S and Rosenfeld A 2012 *J. Laser Appl.* **24** 042006
[31] Ivanov D S *et al* 2015 *Phys. Rev. Appl.* **4** 064006
[32] Ignatov A I, Zhakhovsky V V, Merzlikin A M and Inogamov N A 2019 *J. Phys.: Conf. Ser.* **1147** 012068
[33] Anisimov S I, Prokhorov A M and Fortov V E 1984 *Sov. Phys. Usp.* **27** 181–205
[34] Kanel G I, Razorenov S V and Fortov V E 2004 *Shock-Wave Phenomena and the Properties of Condensed Matter* (New York: Springer-Verlag)
[35] Albertazzi B *et al* 2017 *Sci. Adv.* **3** e160270
[36] Ashitkov S I, Agranat M B, Kanel' G I, Komarov P S and Fortov V E 2010 *JETP Lett.* **92** 516–20
[37] Zhakhovskii V V and Inogamov N A 2010 *JETP Lett.* **92** 521–6
[38] Ashitkov S I, Zhakhovsky V V, Inogamov N A, Komarov P S, Agranat M B and Kanel G I 2017 *AIP Conf. Proc.* **1793** 100035
[39] Ashitkov S I, Komarov P S, Ovchinnikov A V, Struleva E V and Agranat M B 2016 *JETP Lett.* **103** 544–8

[40] Anisimov S I, Imas Ya I, Romanov G S and Khodyko Yu U 1970 *Action of High Power Radiation on Metals* (Moscow: Nauka)

[41] Anisimov S I and Khokhlov V A 1995 *Instabilities in Laser-Matter Interaction* (CRC Press, Inc.)

[42] URL https://www.ipgphotonics.com/ru

[43] Anisimov S I, Kapeliovich B L and Perelman T L 1974 *Sov. Phys. JETP* **39** 375–7

[44] Inogamov N A, Zhakhovskii V V, Ashitkov S I, Petrov Yu V, Agranat M B, Anisimov S I, Nishihara K and Fortov V E 2008 *J. Exp. Theor. Phys.* **107** 1–19

[45] Fabbro R, Fournier J, Ballard P, Devaux D and Virmont J 1990 *J. Appl. Phys.* **68** 775–84

[46] Sokolowski-Tinten K, Bialkowski J, Cavalleri A, von der Linde D, Oparin A, Meyer-ter-Vehn J and Anisimov S I 1998 *Phys. Rev. Lett.* **81** 224–7

[47] Inogamov N A, Petrov Yu V, Anisimov S I, Oparin A M, Shaposhnikov N V, von der Linde D and Meyer-ter-Vehn J 1999 *JETP Lett.* **69** 310–6

[48] Landau L D and Lifshitz E M 1988 *Gidrodinamika* 4th ed (*Theoretical Physics* vol 6) (Moscow: Nauka)

[49] Zeldovich Ya B and Raizer Yu P 1967 *Physics of Shock Waves and High-Temperature Hydrodynamic Phenomena* (Academic Press)

[50] Zhakhovskii V V, Inogamov N A, Petrov Yu V, Ashitkov S I and Nishihara K 2009 *Appl. Surf. Sci.* **255** 9592–6

[51] Demaske B J, Zhakhovsky V V, Inogamov N A and Oleynik I I 2010 *Phys. Rev. B* **82** 064113

[52] Petrov Yu V, Inogamov N A, Zhakhovsky V V and Khokhlov V A 2019 *Contrib. Plasma Phys.* **59** e201800180

[53] Inogamov N A, Khokhlov V A, Petrov Yu V and Zhakhovsky V V 2020 *Opt. Quantum Electron.* **52** 63

[54] Starinskiy S V, Shukhov Y G and Bulgakov A V 2017 *Appl. Surf. Sci.* **396** 1765–74

[55] Kanitz A, Kalus M R, Gurevich E L, Ostendorf A, Barcikowski S and Amans D 2019 *Plasma Sources Sci. Technol.* **28** 103001

[56] Shepelev V V *et al* 2019 *J. Phys.: Conf. Ser.* **1147** 012065

[57] Romashevskiy S A, Ashitkov S I and Agranat M B 2016 *Appl. Phys. Lett.* **109** 261601

[58] Palik E D 1985 *Handbook of Optical Constants of Solids* (Academic)

[59] Johnson P B and Christy R W 1972 *Phys. Rev. B* **6** 4370–9

[60] Babar S and Weaver J H 2015 *Appl. Opt.* **54** 477–81

[61] Ashitkov S I, Komarov P S, Zhakhovsky V V, Petrov Yu V, Khokhlov V A, Yurkevich A A, Ilnitsky D K, Inogamov N A and Agranat M B 2016 *J. Phys.: Conf. Ser.* **774** 012097

[62] Povarnitsyn M E, Itina T E, Sentis M, Khishchenko K V and Levashov P R 2007 *Phys. Rev. B* **75** 235414

[63] Anisimov S I, Inogamov N A, Petrov Yu V, Khokhlov V A, Zhakhovskii V V, Nishihara K, Agranat M B, Ashitkov S I and Komarov P S 2008 *Appl. Phys. A* **92** 939–43

[64] Inogamov N A, Zhakhovskii V V, Ashitkov S I, Khokhlov V A, Petrov Yu V, Komarov P S, Agranat M B, Anisimov S I and Nishihara K 2009 *Appl. Surf. Sci.* **255** 9712–6

[65] Norman G E, Starikov S V and Stegailov V V 2012 *J. Exp. Theor. Phys.* **114** 792–800

[66] Povarnitsyn M E, Andreev N E, Apfelbaum E M, Itina T E, Khishchenko K V, Kostenko O F, Levashov P R and Veysman M E 2012 *Appl. Surf. Sci.* **258** 9480–3

[67] Norman G E, Starikov S V, Stegailov V V, Saitov I M and Zhilyaev P A 2013 *Contrib. Plasma Phys.* **53** 129–39

[68] Inogamov N A, Zhakhovsky V V, Khokhlov V A, Khishchenko K V, Petrov Yu V, Ilnitsky D K and Migdal K P 2014 *Physical Chemical Kinetics in Gas Dynamics* **15** 5

[69] Schäfer C, Urbassek H M and Zhigilei L V 2002 *Phys. Rev. B* **66** 115404

[70] Ivanov D S and Zhigilei L V 2003 *Phys. Rev. B* **68** 064114

[71] Zhigilei L V, Lin Z and Ivanov D S 2009 *J. Phys. Chem. C* **113** 11892–906

[72] Inogamov N A *et al* 2011 *Contrib. Plasma Phys.* **51** 367–74

[73] Demaske B, Zhakhovsky V V, Inogamov N A, White C and Oleynik I I 2013 Split and two-zone elastic-plastic shock waves in nickel: a molecular dynamics study *18th Biennial Intl. Conference of the APS Topical Group on Shock Compression of Condensed Matter held in conjunction with the 24th Biennial Intl. Conference of the Intl. Association for the Advancement of High Pressure Science and Technology (AIRAPT)* vol 58 (Bulletin of the American Physical Society)

[74] Shih C Y, Shugaev M V, Wu C and Zhigilei L V 2017 *J. Phys. Chem. C* **121** 16549–67

[75] Inogamov N A, Khokhlov V A, Petrov Y V and Zhakhovsky V V 2020 *Opt. Quantum Electron.* **52** 63

[76] Whitley V H, McGrane S D, Eakins D E, Bolme C A, Moore D S and Bingert J F 2011 *J. Appl. Phys.* **109** 013505

[77] Inogamov N A, Zhakhovsky V V, Khokhlov V A and Shepelev V V 2011 *JETP Lett.* **93** 226–32

[78] Crowhurst J C, Armstrong M R, Knight K B, Zaug J M and Behymer E M 2011 *Phys. Rev. Lett.* **107** 144302

[79] Zhakhovsky V V, Budzevich M M, Inogamov N A, Oleynik I I and White C T 2011 *Phys. Rev. Lett.* **107** 135502

[80] Inogamov N A *et al* 2012 *AIP Conf. Proc.* **1426** 909–12
[81] Ashitkov S I, Komarov P S, Agranat M B, Kanel G I and Fortov V E 2013 *JETP Lett.* **98** 7
[82] Perriot R, Zhakhovsky V V, Inogamov N A and Oleynik I I 2014 *J. Phys.: Conf. Ser.* **500** 172008
[83] Ashitkov S I, Komapov P S, Agranat M B, Kanel G I and Fortov V E 2014 *J. Phys.: Conf. Ser.* **500** 112006
[84] Zhakhovsky V V, Inogamov N A, Demaske B J, Oleynik I I and White C T 2014 *J. Phys.: Conf. Ser.* **500** 172007
[85] Ashitkov S I, Komarov P S, Struleva E V, Agranat M B and Kanel G I 2015 *JETP Lett.* **101** 276–81
[86] Kanel G I, Zaretsky E B, Razorenov S V, Savinykh A S and Garkushin G V 2017 *AIP Conf. Proc.* **1793** 100030
[87] Kanel G I, Zaretsky E B, Razorenov S V, Ashitkov S I and Fortov V E 2017 *Phys. Usp.* **60** 490–508
[88] Shepelev V V and Inogamov N A 2018 *J. Phys.: Conf. Ser.* **946** 012010